Superhydrophobic surfaces for extreme environmental conditions

Journal Article

Author(s):
Lambley, Henry (iD); Schutzius, Thomas M.; Poulikakos, Dimos

Publication date:
2020-11-03

Permanent link:
https://doi.org/10.3929/ethz-b-000448214

Superhydrophobic Surfaces for Extreme Environmental Conditions

Henry Lambley, Thomas M. Schutzius* and Dimos Poulikakos*

Laboratory of Thermodynamics in Emerging Technologies, Department of Mechanical and

Process Engineering, ETH Zurich, Sonneggstrasse 3, CH-8092 Zurich, Switzerland

Keywords: superhydrophobic, wetting, droplet impact

[*] To whom correspondence should be addressed.

Prof. Dimos Poulikakos

ETH Zurich

Laboratory of Thermodynamics in Emerging Technologies

Sonneggstrasse 3, ML J 36

CH-8092 Zürich

SWITZERLAND

Phone: +41 44 632 27 38

Fax: +41 44 632 11 76

dpoulikakos@ethz.ch

Prof. Thomas Schutzius

Current address:

ETH Zurich

Laboratory for Multiphase Thermofluidics and Surface Nanoengineering

Sonneggstrasse 3, ML J 27.2

CH-8092 Zürich

SWITZERLAND

Phone: +41 44 632 46 04

thomschu@ethz.ch

Abstract

Superhydrophobic surfaces for repelling impacting water droplets are typically created by designing structures with capillary (anti-wetting) pressures greater than those of the incoming droplet (dynamic, water hammer). Recent work has focused on the evolution of the intervening air layer between droplet and substrate during impact, a balance of air compression and drainage within the surface texture, and its role in affecting impalement under ambient conditions through local changes in the droplet curvature. However, little consideration has been given to the influence of the intervening air layer thermodynamic state and composition, in particular when departing from standard atmospheric conditions, on the anti-wetting behaviour of superhydrophobic surfaces. Here, we explore the related physics and determine the working envelope for maintaining robust superhydrophobicity, in terms of the ambient pressure and water vapour content. With single-tier and multitier superhydrophobic surfaces and high-resolution dynamic imaging of the droplet meniscus and its penetration behaviour into the surface texture, we expose a trend of increasing impalement severity with decreasing ambient pressure and elucidate a previously unexplored condensation-based impalement mechanism within the texture resulting from the compression, and subsequent supersaturation, of the intervening gas layer in low pressure, humid conditions. Using fluid dynamical considerations and nucleation thermodynamics, we provide mechanistic understanding of impalement and further employ this knowledge to rationally construct multitier surfaces with robust superhydrophobicity, extending water repellency behaviour well-beyond typical atmospheric conditions. Such a property is expected to find multifaceted use exemplified by transportation and infrastructure applications where exceptional repellency to water and ice is desired.

Significance Statement

Despite the critical role of air in bestowing surfaces with superhydrophobic properties, little consideration has been given to how the atmospheric composition affects the ability of engineered and natural surfaces to repel impinging droplets. We establish that both environmental conditions of reduced pressure and increased humidity can significantly decrease the performance of surfaces which are seemingly robust in ambient conditions. We explain the mechanism behind this by thermodynamically modelling the compressed air layer beneath the droplet immediately before impact and reveal a previously unreported surface failure mechanism stemming from condensation within the texture. We also demonstrate that through the addition of appropriately scaled nanotexture, it is possible to mitigate against the detrimental effects of these extreme environmental conditions.

Introduction

Inspired by nature, microtextured and nanotextured surfaces have demonstrated unique droplet repellent properties(1) which are beneficial for self-cleaning,(2) anti-icing(3) and condensation enhancement.(4) For many practical applications, repelling an impacting water droplet is important. Much work has been performed to understand how surface topography and composition stabilise the Cassie-Baxter wetting state,(5) a prerequisite for high droplet repellency, under static(6, 7) and dynamic(8–24) conditions to preclude transitioning to the Wenzel wetting state.(25) To prevent the Cassie-Baxter-to-Wenzel wetting state transition, hereafter defined as impalement, the capillary (anti-wetting, surface property) pressure must exceed the wetting (droplet) pressure(9, 17). In previous research, the latter has been attributed to the dynamic pressure,(17) effective water hammer(10, 11, 16, 23) and deformation of the droplet by the compressed air layer leading to a ring shaped pressure maximum.(13, 26)

It is established that the use of hierarchical surface texture and low surface energy coatings are key components for achieving liquid repellency and preventing impalement.(13, 15, 16, 27) Much of this understanding is based on work conducted under ambient conditions; however, work on droplet mobility that departs from ambient environmental conditions(28–31), i.e. substrate cooling,(13, 32) supercooled droplet impact,(33, 34) ambient pressure reduction(35–37) and droplet heating,(38) is yielding new insight into, and unveils new requirements for, the rational design of super-repellent surfaces. Mechanisms for the loss of super-repellent behaviour include condensation-based impalement in the presence of hot vapour (warm droplets)(28, 38), increased droplet viscosity(33) and rapid recalescent freezing inhibiting droplet recoil (cold droplets).(32, 34) Therefore, in addition to wettability, it is necessary to investigate important aspects such as non-standard atmosphere environments and nucleation(3, 39, 40)—which affect the intervening

gas layer dynamic state during droplet impact and enhance droplet-substrate adhesion—to enable surface texture tailoring to counter such effects to preserve superhydrophobicity.(38, 41–46) While the effects of droplet and environmental temperature (hot or cold) on superhydrophobicity for impacting droplets are being better understood, research into the effect of the environmental gas pressure, an equally important counterpart, is comparatively scant(35–37); as is the combined effect with humidity. Both are very important for defining the thermodynamic state of the intervening gas layer during droplet impact, necessary to determine its behaviour. Previous work has demonstrated that decreasing the environmental pressure influences the droplet impact dynamics on smooth and rough surfaces (e.g., prompt vs. thin-sheet splashing)(26, 47–50) which may alter impact and recoil dynamics on superhydrophobic surfaces; however, this remains to be seen.

Here we examine, experimentally and theoretically, the combined effects of reducing environmental pressure and varying humidity on droplet impact and recoil from superhydrophobic surfaces, identify novel impalement mechanisms and, armed with this knowledge, rationally nanoengineer robust superhydrophobic surfaces that can repel impacting droplets across a wide range of environmental conditions. We demonstrate that the likelihood of impalement on textured surfaces increases as the ambient pressure decreases and provide rationales to explain this. Additionally, through variation of the relative humidity, we report, and theoretically underpin, a hitherto unknown mechanism for wetting state transition through supersaturation of, and subsequent condensation within, the air layer resulting from the pressure increase beneath an impacting droplet. Finally, we demonstrate an alternative coating capable of resisting impalement within the working envelope experimentally explored, based on our accrued knowledge. We believe that our observations will have profound implications for all applications of

6

superhydrophobicity in both low pressure, such as those involving ice accretion on aircraft through superior repellency of supercooled drops, and naturally humid environments, including for self-cleaning materials such as textiles.

Results & Discussion

To explore the water repellency of superhydrophobic samples to impacting water droplets in extreme environmental conditions (environmental pressure ranging from 0.1 kPa to 100 kPa and relative humidity ranging from 0% to 100%), we synthesised two low surface energy textured coatings: one with single tier roughness and the other with multitier roughness. The single tier roughness surface consisted of transparent polyurethane acrylate (PUA) micropillars replicated on rigid glass substrates using soft-lithography. These were rendered superhydrophobic by depositing a thin uniform layer of a low surface energy fluoroacrylic polymer using initiated chemical vapour deposition (iCVD). This coating does not alter the underlying single tier roughness nature of our micropillared surfaces (see SI Appendix, Table S1). The multitier roughness coating was a nanocomposite which we fabricated by spray coating a dispersion of poly(methyl methacrylate) (PMMA), poly(vinylidene fluoride) (PVDF) and hydrophobic fumed silica nanoparticles (HFS) onto a rigid glass substrate (see Table S2). (For complete information regarding superhydrophobic surface fabrication and characterisation, see Methods, SI Appendix, sections "Details of engineered surfaces used in this study" and "Composition of spray coatings".)

To determine the effect of the ambient pressure, p, and the partial pressure of water vapour, p_v, on substrate performance, droplets of ambient temperature, $T = 23 \pm 1°C$, with initial radius, $R = 1.03 \pm 0.02$ mm, density, ρ_l, and surface tension, σ, were impacted onto a multitier sample with a velocity, $U = 1.17 \pm 0.001$ m s^{-1}. In order to quantify the severity of the droplet impact event, we define the Weber number, $We = 2\rho_l U^2 R / \sigma$, which is the ratio of inertial and surface tension forces. Figure 1a and Figure 1b show image sequences of droplets impacting on our multitier superhydrophobic surface (see inset for a micrograph) with $We = 39$ in environments with $p = 95$ kPa and 0.1 kPa, respectively. In the former case, the droplet rebounds, while in the latter

8

case a large portion of the droplet remains on the surface, demonstrating that environmental pressure can have a major influence on the repellency of a seemingly robust (at atmospheric conditions) superhydrophobic surface. The presence of this remaining, so-called daughter, drop is indicative of impalement and the local transition to a Wenzel wetting state. An intermediate p exists, as can be seen in Figure 1c, at which the receding of the contact line is slowed in comparison to the ambient case but complete rebound is still achieved. The acute necking of the droplet towards the base suggests that the drop has penetrated somewhat into the microtexture, but not sufficiently for the force of adhesion to the texture to overcome the retraction effect of surface tension. However, the introduction of water vapour (relative humidity, $\phi = p_v / p_{v,sat} = 90\%$) into the atmosphere at $p = 9 \text{ kPa}$ yields a contrasting result with a daughter droplet present after rebound (Figure 1d), albeit smaller than for a lower ambient pressure. The full parameter space in which we performed experiments can be seen in Figure 1e. We can divide this parameter space into three zones: impalement, total rebound, and a transition zone in which both aforementioned outcomes are possible. Over the domain tested, p has the greatest influence over the impact event outcome with variations in p_v relevant near the transition zone, in the range $7 \leq p \leq 10 \text{ kPa}$.

The above results prompt further investigations into the transition zone and how both p and p_v affect the probability of impalement, Φ, as well as the size of the daughter droplet. For cases where impalement occurred, we quantified the severity of this by measuring the surface area over which the droplet has fully penetrated the texture—the impaled area—and compromised the superhydrophobicity of the surface, here defined as $\pi D_d^2 / 4$ (Figure 2a). We then normalize the impaled area, $\pi D_d^2 / 4$, by the projected area of the impinging droplet, $\pi D_0^2 / 4$, yielding the normalized impaled area, $\left(D_d / D_0 \right)^2$. The impaled area can be directly related to the work of

9

adhesion of the droplet to the surface, $W_{adh} = (\pi D_d^{\ 2}/4) \times \sigma_{lv}(1+\cos\theta_r^*)$ where θ_r^* is the receding

contact angle, giving the energy required to remove the daughter droplet from the surface. Figure

2b plots Φ vs. p for dry ($p_v \approx 0$ kPa) and humid conditions ($p_v = 2.3$ kPa). From this we see that

decreasing p results in an increase in Φ and that for the same p, increasing p_v also increases Φ.

Figure 2c similarly plots the normalized impaled area, $(D_d/D_0)^2$, vs. p for $p_v \approx 0$ kPa and

$p_v = 2.3$ kPa , respectively. We limit the range of results in the high humidity case as, below

$p_v = 7$ kPa , it is impossible to definitively differentiate between the two impalement mechanisms

which would be simultaneously present. It is clear that decreasing p leads to an increase in

$(D_d/D_0)^2$ and, therefore, the severity of impalement increases. When comparing the humidity

conditions, we found that, despite impalement probability increasing with humidity for the same

environmental pressure (Figure 2b), higher humidity does not have a profound influence on

$(D_d/D_0)^2$ in the pressure range $7 \le p \le 9$ kPa . We attribute this to the region of influence of the

intervening air layer (whose magnitude is a function of the ambient pressure only) on both humidity

and pressure-based impalement mechanisms studied.

To explore the different impalement mechanisms observed, we visualised the droplet-

surface interactions during impact from below with an inverted microscope and high-speed camera

(see Methods, SI Appendix, section "Experimental Setup" and Figure S1 for more details). For

this, we fabricated transparent PUA micropillar substrates, with precisely controlled single tier

texture, of diameter, pitch and height: $[d,s,h] = [2.5,5.0,5.8]$ μm . Again, we released droplets

from above the sample under a range of environmental conditions and a moderate value of $We = 48$

. Figure 3a contains an image sequence of a water droplet impacting on, spreading and recoiling

from a single tier superhydrophobic surface for $[p, p_v] = [95,1.3]$ kPa (atmospheric pressure and

moderately humid). It is interesting to note the wetting behaviour of the droplet 2.2 ms after contact, when it is fully spread. Here one can see two concentric dark thin rings (approximate diameters are 0.22 and 0.72 mm; see magnified inset and schematic), which is characteristic of the displacement of the air layer within the surface texture and, therefore, partial impalement. We also show bottom-view and extrapolated side-view schematics to illustrate the behaviour of the meniscus, which is partially penetrating the surface texture within these rings. On the inside of the inner ring, there is a bubble formed, which is consistent with previous work(13, 26, 51). The bubble drains as the contact line recedes, the meniscus withdraws from the surface texture and, at $t = 12.5$ ms, we observe full rebound. Figure 3b and Figure 3c contain image sequences of droplets impacting on the single tier superhydrophobic surface at $[p, p_v] = [2.5, \approx 0]$ kPa (medium-vacuum, dry) and $[p, p_v] = [2.5, 2.3]$ kPa (medium-vacuum, humid), respectively. In Figure 3b, the droplet rebounds while in Figure 3c, the droplet impales; the difference between the two cases is that in the impalement case, the ring region within which the droplet meniscus penetrates the surface is much thicker and darker, indicating more air has been displaced and the bottom of the cavity has been wetted. This contact area is large enough for the force of adhesion to overcome the surface tension with part of the droplet left behind. We hypothesise, and pursue this hypothesis below, that the reversal of outcome due solely to a change in the surrounding gas humidity, can be explained by gas compression, supersaturation and subsequent condensation of water vapour within the texture, which bridges to the droplet meniscus. The increased Φ in high ambient humidity conditions suggests that the vapour necessary for condensation-based impalement is supplied by the environment and not the evaporating droplet itself.

In order to understand the mechanism responsible for condensation-based impalement, we model how changes in pressure, Δp_g, and temperature, ΔT_g, within the intervening gas layer evolve

11

during droplet impact and use this to determine the vapour supersaturation and water condensation rates. First, we focus on estimating Δp_g using an appropriate model based on calculating the dimple height, width and formation time. Figure 4a gives a schematic of a droplet approaching a flat substrate with velocity, U. The gas layer beneath the droplet is displaced and begins to drain outwards with a velocity U_r. Prior to substrate contact, Δp_g can rise significantly, exceeding the internal pressure of the droplet and causing the bottom of the droplet to stagnate and deform, first flattening and then developing a dimple. The height and width of the region under the dimple are defined as H and L, respectively, and we can write $L \sim (RH)^{1/2}$ from geometrical considerations(26, 51).

Initially, far from the substrate, the air layer drains without compressing yielding $\Delta p_{g,incomp} \sim \mu_g UR / H^2$ (26, 51) (incompressible, lubrication approximation(52), $H/L \ll 1$) where μ_g is the gas dynamic viscosity. We choose to neglect the specific gas layer composition as the viscosity of water vapour is similar to that dry air. However, if the impact conditions require a significant pressure build up to arrest the droplet, compressibility effects cannot be ignored(53). We choose to include these when Δp_g is of the same order as p or, equivalently, at a critical air layer thickness $H_c = R(\mu_g U / Rp)^{1/2}$ (26). Beyond this point, we can make the simplification that compression of the air layer dominates drainage (assuming $\Delta p_g \gg p$), yielding $\Delta p_g \sim p(H_c / H)^k$ where k is the polytropic index. We can balance this with the inertial pressure gradient within the liquid (neglecting surface tension effects)(51, 54), given by $\Delta p_l / L = \rho_l U^2 / H$, which yields a compressible final dimple height at contact with the substrate of

$$H_d = \beta R S^{2/3} \varepsilon^{(2-k)/(2k-1)} \tag{1}$$

12

where $S = \mu_\text{g} / (\rho_\text{l} U R)$ is the Stokes number, $\varepsilon = p / (R\mu_\text{g}^{-1} U^7 \rho_\text{l}^4)^{1/3} \leq 1$ is a compressibility factor (in the incompressible limit, $\varepsilon = 1$) and β is a scaling factor, that is a function of ε and k, calculated using previously reported simulations(26) (for a complete description of the analysis performed, see SI Appendix, section "Intervening Vapour Layer Analysis"). We can then calculate the maximum overpressure (above the atmospheric pressure, p) in the intervening gas layer as

$$\Delta p_\text{g}^* = \frac{p}{\beta^k \, \varepsilon^{k((2-k)/(2k-1)+0.5)}}. \tag{2}$$

To determine the maximum value of ΔT_g at impact, ΔT_g^*, we evaluate the diffusion of heat into the substrate from the gas layer during compression. For our experimental conditions, we calculate that $H_\text{d} \sim O(10^{-6}\ \text{m})$, yielding a timescale for dimple formation of $\tau_\text{d} \sim H_\text{d} / U \sim 10^{-6}\ \text{s}$ ($R = 1.03\ \text{mm}$, $\mu_\text{g} = 1.83 \times 10^{-5}\ \text{Pa s}$, $U = 1.30\ \text{m s}^{-1}$). The thermal penetration depth in this time can be approximated as $l \sim (\tau_\text{d} \alpha_\text{PUA})^{1/2}$, where α_PUA is the thermal diffusivity of the PUA substrate. Comparing the thermal capacitances, C, of the gas layer and thermal penetration layer(55), we find that $C_\text{PUA} / C_\text{g} = \rho_\text{PUA} c_\text{PUA} l / \rho_\text{g} c_\text{g} H_\text{d} \sim O(10^3)$, where c is the specific heat, suggesting that any additional heat generated through compression is readily and immediately absorbed by the substrate; making an isothermal compression approximation valid (*i.e.* $\Delta T_\text{g}^* = 0$, $\therefore k = 1$).

For a given value of *We* and p, by fixing R, σ, ρ_l and μ_g, we can calculate U, S, ε, and, therefore, Δp_g^*. In Figure 4b, a plot of p vs. *We* vs. $\Delta p_\text{g}^* / p$, we see that for high values of *We* and low values of p, that $\Delta p_\text{g}^* / p$ can become quite large. For example, for $p = 2.5\ \text{kPa}$ and $We = 48$ (the experimental conditions for impalement from Figure 3c) we obtain $\Delta p_\text{g}^* / p \approx 7$. With Δp_g^*

and ΔT_g^* established, we proceed with calculating the water vapour supersaturation, ϕ_g, in the intervening gas layer, which is defined as the ratio of p_v in the intervening gas layer to the saturation value of p_v at conditions of $p + \Delta p_g^*$ and T. Using the definition of ϕ, we can also define it as $\phi_g = \phi(1 + \Delta p_g^* / p)$. In Figure 4c, a plot of $\Delta p_g^* / p$ vs. ϕ vs. ϕ_g, we see that for high values of $\Delta p_g^* / p$ and ϕ, that ϕ_g can become significant ($\phi_g \gg 1$). For the regime in which we performed low pressure experiments ($p = 2.5$ kPa, $We = 48$, $\Delta p_g^* / p \approx 7$, $\phi \approx 90\%$), we calculate very high degrees of supersaturation, ($\phi_g \approx 7.2$).

Before calculating the nucleation rate of droplets within the surface texture which displace the intervening air layer and promote impalement, we first need to understand how long the pressure remains elevated in the gas layer. As a first approximation, we suggest that this will be on the same order as the compression, $\tau_c \sim (H_c - H_d)/U \sim O(10^{-6} \text{ s})$, due to the rapid drainage of the compressed intervening air layer through the surface texture (for the full discussion and calculations, see SI Appendix, section "Dimple Drainage Model"). From ϕ_g, we can determine the condensation nucleation rate: $J = J_0 \exp(-\Delta G_{het}^* / k_B T)$ where J_0 is the kinetic constant, ΔG_{het}^*, a function of ϕ_g and surface characteristics, is the critical free energy barrier to heterogeneous nucleation, and k_B is the Boltzmann constant (see SI Appendix, section "Nucleation Rate Model"). In Figure 4d, a plot of J vs. S, we see that for $\phi_g \geq 5$, J exceeds 1 μm^{-2} μs^{-1}, a nucleation density much greater than that of the micropillars. For $\phi_g = 7.2$, we calculate $J \sim O(10^3 \ \mu m^{-2} \ \mu s^{-1})$. Multiplying that by the area of one pillar cell, $A = s^2 + \pi dh$, and τ_c, we can calculate the number of embryos formed in a single unit cell of the micropillars while the gas is compressed as

$N = JA\tau_Q \sim 10^5$ embryos. In contrast, for the same impact at low humidity we calculate $N \sim 10^{-51}$

embryos per unit cell per impact ($\Delta p_g^* / p \approx 7$, $\phi \approx 25\%$). This explains the promoting effect of

humidity on the tendency of impacting droplets to impale.

Next, we explore the mechanism responsible for impalement at reduced pressures and low

relative humidity. To account for the overestimation of impalement resistance when balancing the

dynamic pressure of an impinging droplet with the capillarity of a superhydrophobic surface,

previous works have suggested both a water hammer effect[23] and enhanced droplet curvature

resulting from a pressure build up beneath the droplet immediately before impact[13] as possible

mechanisms. For the former, the presence of an intervening air layer might abate any shock formed

on impact whereas for the latter, removing this could inhibit the droplet deformation and prevent

impalement. To our knowledge, an increased likelihood of impalement at reduced pressures has

not been demonstrated before with previous work even suggesting that the ambient pressure has

no effect up to a Weber number of 150[35]. To elucidate the correlation of increased impalement

severity with reducing ambient pressure, we now analyse the effect of p on the size of the dimple

that forms during impact. We have already seen that the height of the dimple is a function of p

(Equation (1)). Owing to compressibility effects ($\varepsilon < 1$), we calculate that decreasing p reduces H_d

(Figure 5a). Whilst we were unable to directly quantify H_d experimentally, we sought to verify our

conjecture by measuring the final dimple width, L_d (which scales as $\left(RH_d\right)^{1/2}$) at different pressures

(Figure 5b,c), noting the large difference in L_d between ambient ($p = 95$ kPa, $L_d = 0.32 \pm 0.04$ mm

) and medium vacuum ($p = 2.5$ kPa, $L_d = 0.16 \pm 0.02$ mm) experimental conditions. In Figure 5c,

we were able to verify the proposed scaling relation by fitting our experimental data with

$L_d = a(RH_d)^{1/2}$ using a scaling prefactor of $a = 8$ and values of H_d calculated from Equation 1.

With a smaller H_d, the air "cushion" built up beneath the droplet before impact is abated leading to a firmer impact with the surface and reduced resistance to meniscus advancement between the asperities. To evaluate a critical thickness when the reduction in compressed gas cushion thickness is sufficiently large to enhance the probability of impalement, we compare H_d to the molecular mean free path of the gas, $\lambda = k_B T / \sqrt{2} \pi d_g^2 p$, where d_g is the kinetic diameter of the gas molecules, by defining a gas cushion thickness coefficient, $\delta = H_d / \lambda$ – an inverse Knudsen number. As δ approaches unity, the droplet will locally come into contact with the substrate – in our case the tops of the pillars – preventing the dissipation of any kinetic energy before impact, making impalement more favourable. Plotting δ over a range of p and We (Figure 5c), we see that this crossover of regime is found at $p \sim O(10^1 \text{ kPa})$, similar to the impalement criterion for our multitier polymer nanocomposite substrate exposed in Figure 1e. Without the air cushion, the mechanism of impalement is then analogous to the previous applications of the water hammer effect to textured surfaces(10, 11, 23), which propose scaling factors, $k_{WH} < 1$, of the pressure increase due to water hammer, $p_{WH} = k_{WH} \rho_l U c$ where c is the speed of sound in water, to account for dissipation owing to compression of the air layer and the timescale over which the meniscus advances through the texture.

Now that we have proposed mechanisms for droplet impalement on superhydrophobic surfaces under extreme pressure and humidity conditions, we now explore the possibility of using this knowledge to design robust superhydrophobic surfaces. Recent molecular and density functional theory simulation work has suggested that nanoscale effects such as density fluctuations and fluid-wall interactions can lead to spontaneous de-wetting of filled nanocavities (i.e. Wenzel to Cassie-Baxter transition) via non-classical transition pathways allowing for surfaces for which

the de-wetted state is stabilized and energetically favourable at the nanoscale as well as proposing that stable superhydrophobic surfaces can be realized when combining these endlessly dry nanocavities with microtexture as part of hierarchical structures(56–58). Additionally, previous condensation work has indicated that dense nanotexture on surfaces can facilitate condensation nuclei growth out of the nanotexture, forming a largely Cassie-Baxter wetting state, which has low substrate adhesion(41, 45, 59, 60). For this, the roughness features (e.g. wire diameter, particle diameter, etc.) need to have a length scale, $2r_s$, that is similar to, or smaller than, the condensing droplet(43, 59). We can determine the diameter of the condensing droplets by calculating the critical embryo size for condensation nucleation, $2r^*$, which depends on ϕ_g. For $\phi_g = [1.5, 7.2]$, we find that $r^* = [2.6, 0.5]$ nm respectively, and suggests that $r_s = O(1) - O(10)$ nm is the range of surface texture feature sizes that are necessary to influence the wetting behaviour of condensing droplets and achieve low-adhesion Cassie-Baxter wetting states. To achieve this in a facile manner, we used the spray coating of a suspension of HFS nanoparticles in ethanol onto the bare PUA micropillars resulting in a uniform layer of sub-micron features that did not affect the overall topography of the microtexture (for full details see Methods and SI Appendix, Table S2). With a primary roughness length scale, r_{HFS}, of 8.5 nm for the particles used (BET specific surface area of 160 m^2 g^{-1}, particles approximated as spheres) , we expect that this facile and scalable process will promote composite wetting condensation for all but the most extreme supersaturations; noting that these would not be sustained for an appreciable amount of time. In Figure 6a, the impact conditions ($We = 63$, $[p, p_v] = [2.5, \approx 0]$ kPa) corresponding to the failure of our bare micropillars (see SI Appendix, Figure S3b) are directly replicated for our hierarchical micropillars. We see full rebound of the droplet with minimal penetration of the meniscus into the texture demonstrating that addition of nanotexture also serves to mitigate against pressure-based effects as the air cushion

17

thickness requirement to prevent impalement is significantly lower for smaller and denser textures. The overall contact time of the droplet is reduced owing to the reduced contact angle hysteresis (see SI Appendix, Table S1) imparted by the additional layer of texture. This less homogeneous roughness results in the contact line receding at different rates but does not affect the overall repellency of the surface. In Figure 6b, a very similar result for the complementary high humidity case ($[p, p_v] = [2.5, 2.3]$ kPa) can be seen; verifying that the nanotexture has limited the adhesion of condensate nuclei growing throughout the texture, prohibiting impalement.

Conclusions

We have elucidated impalement failure mechanisms for droplets impinging on superhydrophobic surfaces under environmental conditions markedly departing from those of standard atmosphere. Through measurements, visual observation and a predictive model, we have established that compressibility of the air layer at low p leads to smaller volumes of air entrained on impact resulting in reduced cushioning of the droplet and p_{WH} which are sufficient to overcome the capillary pressure at lower values of We. Further, we have exposed a hitherto unknown condensation-based impalement mechanism for droplets in a high p_{v} environment due to compression and supersaturation of the intervening air layer immediately before impact. Finally, we have used the knowledge gathered to mitigate against these failure mechanisms and demonstrated a facile modification to our existing micropillar structures capable of extending the material working envelope. These exciting findings could have profound implications on the design of superhydrophobic surfaces for reduced pressure and humid environment applications including mitigating against ice accretion from supercooled droplets in the context of aviation and towards robust self-cleaning textiles.

Methods

Materials

Microscope slides (75 x 25 mm) were purchased from VWR. We obtained Polydimethylsiloxane (PDMS) silicone elastomer and curing agent (Sylgard® 184, 10:1 ratio) from The Dow Chemical Company and a UV-curable polyurethane acrylate (PUA) resin (MINS-311RM) from Minuta Technology. Trichlorovinylsilane (TCVS) 1H,1H,2H,2H-perfluorodecyl acrylate (PFDA), *tert*-butylperoxide (TBPO), 1-methyl-2-pyrrolidinone (NMP), poly(methyl methacrylate) (PMMA) and poly(vinylidene fluoride) (PVDF) were purchased from Sigma-Aldrich. We obtained hydrophobic fumed silica nanoparticles (HFS, Aerosil R8200, BET Surface Area 160 ± 25 m^2 g^{-1}) from Evonik.

Preparation

To create the multitier superhydrophobic coating, glass slides were spray-coated with a superhydrophobic polymer/HFS solution as described in ref. (61). Two stock solutions of 10 wt% PMMA in acetone and PVDF in NMP were produced by overnight mechanical mixing at room temperature and 50°C respectively. A further suspension of HFS R8200 was made by combing 500 mg of particles and 6700 mg of acetone and probe-sonicating for 30 s. 500 mg of 10 wt% PMMA and PVDF were each added to the HFS suspension and mechanically mixed for 30 min. We deposited this mixture using an airbrush (Paasche VL, 0.73 mm head) using compressed air at 3 bar from a distance of ~20 cm. To remove the solvents, the coatings were dried on a hot plate at 100°C for 15 min.

To produce transparent micropillars, we replicated a silicon master etched with DRIE Bosch process using soft-lithography. PDMS and the curing agent at a 10:1 ratio were mixed and

degassed under vacuum to remove air bubbles. This was poured over the master and degassed again before curing in an oven at 70°C for 2 h. After demoulding the PDMS negative, smaller portions of the mould were placed on top of PUA coated glass slide which were degassed and cured in a UV chamber (Gie-Tec GmbH) for 10 min; followed by a final demoulding. These were then rendered superhydrophobic using an iCVD deposition of a hydrophobic poly(perfluorodecyl acetate) pPFDA coating comprising a PFDA monomer and TBPO initiator preceded by CVD of TCVS to enable binding of the coating to the PUA.

Characterization

The topography of the surfaces was characterised using scanning electron microscopy (SEM) and stylus profilometry (Bruker Dektak XT). For SEM micrographs, a 2nm thickness layer of Pt was sputtered to reduce charge build up. Acceleration voltages of between 0.5 and 2 kV were used with secondary electron detectors. Advancing and receding contact angles were measured using a goniometer (OCA 35, DataPhysics) with a titling stage and droplet volume of 10 μl.

Experimental setup and protocols

The environmental chamber was evacuated and dried to an ambient pressure below the limit of the pressure sensor used ($p \leq 0.01$ kPa). Dry gaseous nitrogen and water vapour evaporated from a small vile were then added to create the desired environmental conditions. Droplets were introduced into the chamber via a needle positioned above the sample connected to a syringe pump. A sufficiently low flow rate was used to allow droplets to detach under gravity with negligible pressure force. The surface was dried after every experiment *in situ* using a 15 s burst of dry gaseous nitrogen from ~2 cm distance. Image analysis was performed using MATLAB to obtain impact *We* values and daughter droplet sizes.

Impacts were visualised from either the side or bottom (through a reflectance microscope) using a Photron SA1.1 high speed camera at 8000 and 10000 frames per second respectively. Side-view experiment were illuminated from behind the droplet using a diffuse white LED source (Advanced Illuminations). Bottom-view experiments were illuminated by a collimated, narrow-band driven LED (peak wavelength 450 nm, ThorLabs).

Data Availability

All data and codes used to produce this article can be found in the ETH Research Collection at https://doi.org/10.3929/ethz-b-000432012. Original videos files too large to be uploaded are available upon reasonable request.

SI Appendix

The following SI Appendix sections are included: Details of engineered surfaces used in this study, Composition of spray coatings, Experimental Setup, Intervening Vapour Layer Analysis, Intervening Vapour Layer Analysis, Nucleation Rate Model and Higher *We* Experiments.

Author contributions statement

T.M.S. and D.P. designed the research and supervised all its aspects. H.L. fabricated and characterised surfaces, performed experiments, analysed data and implemented the theoretical model. H.L., T.M.S. and D.P. wrote the paper.

Acknowledgements

thank Peter Feusi and Jovo Vidic for technical support and Efstratios Mitridis for help with microfabrication.

Additional information

References

1. D. Quéré, Non-sticking drops. *Reports Prog. Phys.* **68**, 2495–2532 (2005).

2. W. Barthlott, C. Neinhuis, Purity of the sacred lotus, or escape from contamination in biological surfaces. *Planta* **202**, 1–8 (1997).

3. T. M. Schutzius, *et al.*, Physics of icing and rational design of surfaces with extraordinary icephobicity. *Langmuir* **31**, 4807–4821 (2015).

4. J. B. Boreyko, C.-H. Chen, Self-Propelled Dropwise Condensate on Superhydrophobic Surfaces. *Phys. Rev. Lett.* **103**, 184501 (2009).

5. A. B. D. Cassie, S. Baxter, Wettability of porous surfaces. *Trans. Faraday Soc.* **40**, 546–551 (1944).

6. A. Marmur, Wetting on hydrophobic rough surfaces: To be heterogeneous or not to be? *Langmuir* **19**, 8343–8348 (2003).

7. N. A. Patankar, Consolidation of hydrophobic transition criteria by using an approximate energy minimization approach. *Langmuir* **26**, 8941–8945 (2010).

8. B. He, N. A. Patankar, J. Lee, Multiple equilibrium droplet shapes and design criterion for rough hydrophobic surfaces. *Langmuir* **19**, 4999–5003 (2003).

9. A. Lafuma, D. Quéré, Superhydrophobic states. *Nat. Mater.* **2**, 457–460 (2003).

10. H. M. Kwon, A. T. Paxson, K. K. Varanasi, N. A. Patankar, Rapid deceleration-driven wetting transition during pendant drop deposition on superhydrophobic surfaces. *Phys. Rev. Lett.* **106**, 1–4 (2011).

11.　S. Dash, M. T. Alt, S. V. Garimella, Hybrid surface design for robust superhydrophobicity. *Langmuir* **28**, 9606–9615 (2012).

12.　P. Papadopoulos, L. Mammen, X. Deng, D. Vollmer, H. Butt, How superhydrophobicity breaks down. *Proc. Natl. Acad. Sci. U. S. A.* **110**, 3254–3258 (2013).

13.　T. Maitra, *et al.*, On the Nanoengineering of Superhydrophobic and Impalement Resistant Surface Textures below the Freezing Temperature. *Nano Lett.* **14**, 172–182 (2014).

14.　T. Vasileiou, J. Gerber, J. Prautzsch, T. M. Schutzius, D. Poulikakos, Superhydrophobicity enhancement through substrate flexibility. *Proc. Natl. Acad. Sci.* **113**, 13307–13312 (2016).

15.　C. Peng, Z. Chen, M. K. Tiwari, All-organic superhydrophobic coatings with mechanochemical robustness and liquid impalement resistance. *Nat. Mater.* **17**, 355–360 (2018).

16.　M. McCarthy, *et al.*, Biotemplated hierarchical surfaces and the role of dual length scales on the repellency of impacting droplets. *Appl. Phys. Lett.* **100**, 1–6 (2012).

17.　D. Bartolo, *et al.*, Bouncing or sticky droplets: Impalement transitions on superhydrophobic micropatterned surfaces. *Europhys. Lett.* **74**, 299–305 (2006).

18.　M. Reyssat, A. Pépin, F. Marty, Y. Chen, D. Quéré, Bouncing transitions on microtextured materials. *Europhys. Lett.* **74**, 306–312 (2006).

19.　S. Moulinet, D. Bartolo, Life and death of a fakir droplet: Impalement transitions on superhydrophobic surfaces. *Eur. Phys. J. E* **24**, 251–260 (2007).

20.　J. Hyväluoma, J. Timonen, Impalement transitions in droplets impacting microstructured

superhydrophobic surfaces. *Europhys. Lett.* **83** (2008).

21. Y. C. Jung, B. Bhushan, Dynamic effects of bouncing water droplets on superhydrophobic surfaces. *Langmuir* **24**, 6262–6269 (2008).

22. J. Hyväluoma, J. Timonen, Impact states and energy dissipation in bouncing and non-bouncing droplets. *J. Stat. Mech. Theory Exp.* **2009** (2009).

23. T. Deng, *et al.*, Nonwetting of impinging droplets on textured surfaces. *Appl. Phys. Lett.* **94**, 133109 (2009).

24. T. Koishi, K. Yasuoka, S. Fujikawa, T. Ebisuzaki, X. C. Zeng, Coexistence and transition between Cassie and Wenzel state on pillared hydrophobic surface. *Proc. Natl. Acad. Sci.* **106**, 8435–8440 (2009).

25. R. N. Wenzel, Resistance of Solid Surfaces To Wetting by Water. *Ind. Eng. Chem.* **28**, 988–994 (1936).

26. S. Mandre, M. Mani, M. P. Brenner, Precursors to splashing of liquid droplets on a solid surface. *Phys. Rev. Lett.* **102**, 4–7 (2009).

27. X. M. Li, D. Reinhoudt, M. Crego-Calama, What do we need for a superhydrophobic surface? A review on the recent progress in the preparation of superhydrophobic surfaces. *Chem. Soc. Rev.* **36**, 1350–1368 (2007).

28. Y. T. Cheng, D. E. Rodak, Is the lotus leaf superhydrophobic? *Appl. Phys. Lett.* **86**, 1–3 (2005).

29. Y. T. Cheng, D. E. Rodak, C. A. Wong, C. A. Hayden, Effects of micro- and nano-structures on the self-cleaning behaviour of lotus leaves. *Nanotechnology* **17**, 1359–1362

(2006).

30.   K. A. Wier, T. J. McCarthy, Condensation on ultrahydrophobic surfaces and its effect on droplet mobility: Ultrahydrophobic surfaces are not always water repellant. *Langmuir* **22**, 2433–2436 (2006).

31.   K. K. Varanasi, T. Deng, J. D. Smith, M. Hsu, N. Bhate, Frost formation and ice adhesion on superhydrophobic surfaces. *Appl. Phys. Lett.* **97**, 95–98 (2010).

32.   L. Mishchenko, *et al.*, Design of Ice-free Nanostructured Surfaces Based on Repulsion of Impacting Water Droplets. *ACS Nano* **4**, 7699–7707 (2010).

33.   T. Maitra, *et al.*, Supercooled water drops impacting superhydrophobic textures. *Langmuir* **30**, 10855–10861 (2014).

34.   T. Vasileiou, T. M. Schutzius, D. Poulikakos, Imparting Icephobicity with Substrate Flexibility. *Langmuir* **33**, 6708–6718 (2017).

35.   P. Tsai, S. Pacheco, C. Pirat, L. Lefferts, D. Lohse, Drop impact upon micro- and nanostructured superhydrophobic surfaces. *Langmuir* **25**, 12293–12298 (2009).

36.   P. Tsai, R. C. A. Van Der Veen, M. Van De Raa, D. Lohse, How micropatterns and air pressure affect splashing on surfaces. *Langmuir* **26**, 16090–16095 (2010).

37.   T. M. Schutzius, *et al.*, Spontaneous droplet trampolining on rigid superhydrophobic surfaces. *Nature* **527**, 82–85 (2015).

38.   T. Mouterde, *et al.*, Two recipes for repelling hot water. *Nat. Commun.* **10**, 1–7 (2019).

39.   C. Walker, *et al.*, Desublimation frosting on nanoengineered surfaces. *ACS Nano* **12**,

8288–8296 (2018).

40. K. K. Varanasi, M. Hsu, N. Bhate, W. Yang, T. Deng, Spatial control in the heterogeneous nucleation of water. *Appl. Phys. Lett.* **95**, 2007–2010 (2009).

41. C. H. Chen, *et al.*, Dropwise condensation on superhydrophobic surfaces with two-tier roughness. *Appl. Phys. Lett.* **90** (2007).

42. K. Rykaczewski, *et al.*, How nanorough is rough enough to make a surface superhydrophobic during water condensation? *Soft Matter* **8**, 8786 (2012).

43. K. Rykaczewski, *et al.*, Multimode multidrop serial coalescence effects during condensation on hierarchical superhydrophobic surfaces. *Langmuir* **29**, 881–891 (2013).

44. T. Mouterde, *et al.*, Antifogging abilities of model nanotextures. *Nat. Mater.* **16**, 658–663 (2017).

45. R. Enright, N. Miljkovic, A. Al-Obeidi, C. V. Thompson, E. N. Wang, Condensation on superhydrophobic surfaces: The role of local energy barriers and structure length scale. *Langmuir* **28**, 14424–14432 (2012).

46. C. Hao, *et al.*, Bioinspired Interfacial Materials with Enhanced Drop Mobility: From Fundamentals to Multifunctional Applications. *Small* **12**, 1825–1839 (2016).

47. L. Xu, W. W. Zhang, S. R. Nagel, Drop splashing on a dry smooth surface. *Phys. Rev. Lett.* **94**, 1–4 (2005).

48. L. Xu, L. Barcos, S. R. Nagel, Splashing of liquids: Interplay of surface roughness with surrounding gas. *Phys. Rev. E* **76**, 1–5 (2007).

49. A. Latka, A. Strandburg-Peshkin, M. M. Driscoll, C. S. Stevens, S. R. Nagel, Creation of prompt and thin-sheet splashing by varying surface roughness or increasing air pressure. *Phys. Rev. Lett.* **109**, 3–6 (2012).

50. A. L. Yarin, Drop Impact Dynamics: Splashing, Spreading, Receding, Bouncing…. *Annu. Rev. Fluid Mech.* **38**, 159–192 (2006).

51. W. Bouwhuis, *et al.*, Maximal air bubble entrainment at liquid-drop impact. *Phys. Rev. Lett.* **109**, 2–5 (2012).

52. P.-G. de Gennes, F. Brochard-Wyart, D. Quéré, *Capillarity and Wetting Phenomena* (Springer New York, 2004).

53. P. D. Hicks, R. Purvis, Air cushioning in droplet impacts with liquid layers and other droplets. *Phys. Fluids* **23** (2011).

54. M. Mani, S. Mandre, M. P. Brenner, Events before droplet splashing on a solid surface. *J. Fluid Mech.* **647**, 163–185 (2010).

55. S. Mandre, M. P. Brenner, The mechanism of a splash on a dry solid surface. *J. Fluid Mech.* **690**, 148–172 (2012).

56. A. Giacomello, L. Schimmele, S. Dietrich, M. Tasinkevych, Recovering superhydrophobicity in nanoscale and macroscale surface textures. *Soft Matter* **15**, 7462–7471 (2019).

57. S. Meloni, A. Giacomello, C. M. Casciola, Focus Article: Theoretical aspects of vapor/gas nucleation at structured surfaces. *J. Chem. Phys.* **145**, 211802 (2016).

58. S. Prakash, E. Xi, A. J. Patel, Spontaneous recovery of superhydrophobicity on

nanotextured surfaces. *Proc. Natl. Acad. Sci. U. S. A.* **113**, 5508–5513 (2016).

59. C. Lv, P. Hao, X. Zhang, F. He, Dewetting Transitions of Dropwise Condensation on Nanotexture-Enhanced Superhydrophobic Surfaces. *ACS Nano* **9**, 12311–12319 (2015).

60. X. Chen, *et al.*, Nanograssed Micropyramidal Architectures for Continuous Dropwise Condensation. *Adv. Funct. Mater.* **21**, 4617–4623 (2011).

61. T. Vasileiou, J. Gerber, J. Prautzsch, T. M. Schutzius, D. Poulikakos, Superhydrophobicity enhancement through substrate flexibility. *Proc. Natl. Acad. Sci.* **113**, 13307–13312 (2016).
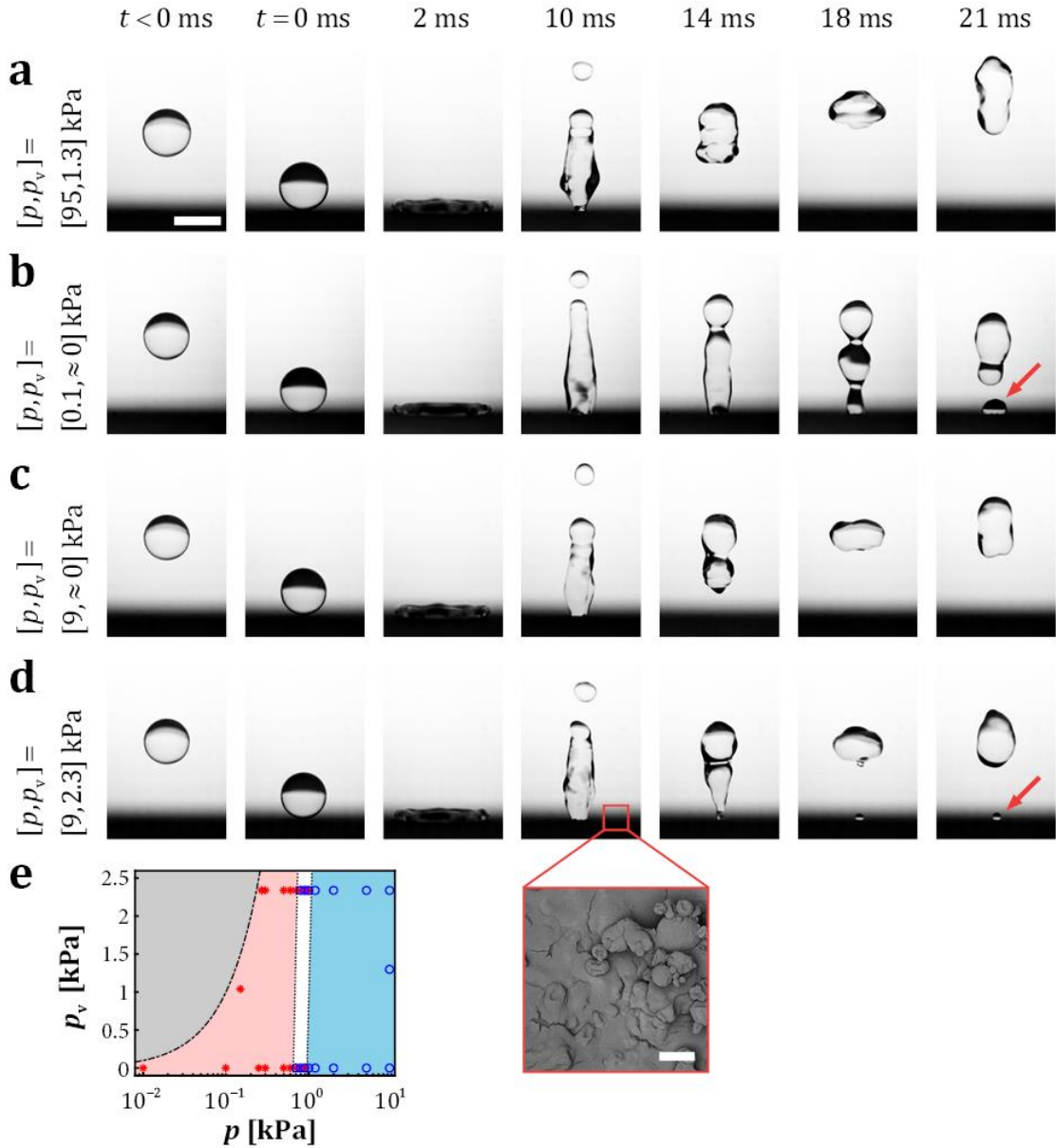
Figure 1. Droplet impact on superhydrophobic surfaces with multitier surface texture in varying atmospheric conditions ($We = 39$). Side-view impact sequences for different environmental conditions: **(a)** high pressure, moderately humid ($[p, p_v] = [95, 1.3]$ kPa), **(b)** medium vacuum, dry ($[p, p_v] = [0.1, \approx 0]$ kPa), **(c)** low vacuum, dry ($[p, p_v] = [9, \approx 0]$ kPa), and **(d)** low vacuum, humid ($[p, p_v] = [9, 2.3]$ kPa). Impalement in **b** and **d** is defined by the presence of a daughter droplet on the surface after rebound and is indicated by red arrows. Inset in **d**: Micrograph of the multitier superhydrophobic surface. **(e)** Plot of p_v *vs.* p *vs.* impalement (red star) or rebound (blue circle). A transition zone exists within which, both outcomes are possible (white region). The black line of $p_v = p$ bounds the impossible to access grey region in which $p_v > p$. Individual

data points have $n \geq 5$; the red, white, and blue domains have a total of $N(\text{red,white,blue}) = (80,100,60)$ respectively. Scale bars: (a)-(d) 2 mm; micrograph, 20 µm.
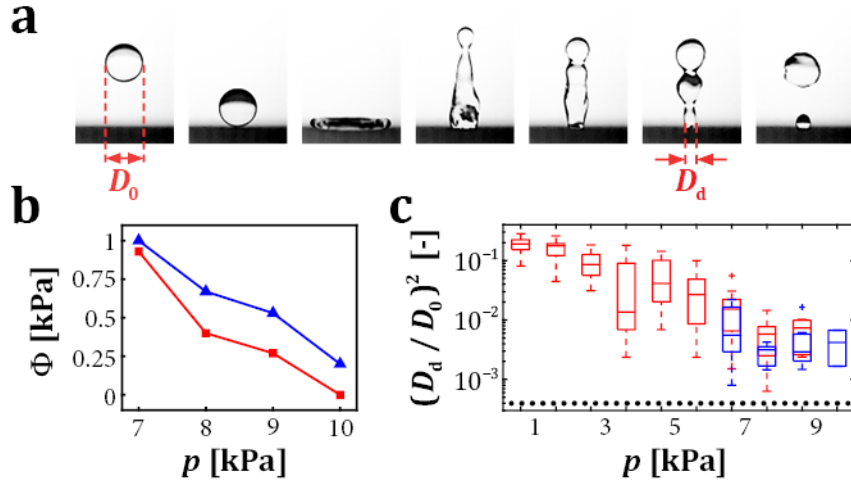
Figure 2. Properties of impalement. **(a)** Side-view impact sequence of a typical impalement case ($We = 39$) defining initial droplet diameter area, D_0, and daughter droplet impaled diameter, D_d. **(b)** Plot of the probability of impalement, Φ, vs. p for $p_\mathrm{v} \approx 0\ \mathrm{kPa}$ (red line) and $p_\mathrm{v} = 2.3\ \mathrm{kPa}$ (blue line). Individual data points have $n \geq 10$. **(c)** Box plot of normalized impaled area, $(D_\mathrm{d}/D_0)^2$, vs. p for $p_\mathrm{v} \approx 0\ \mathrm{kPa}$ (red) ($n = 15$) and $p_\mathrm{v} = 2.3\ \mathrm{kPa}$ (blue) ($n \geq 10$). The dotted line corresponds to the resolution limit of our measurements.
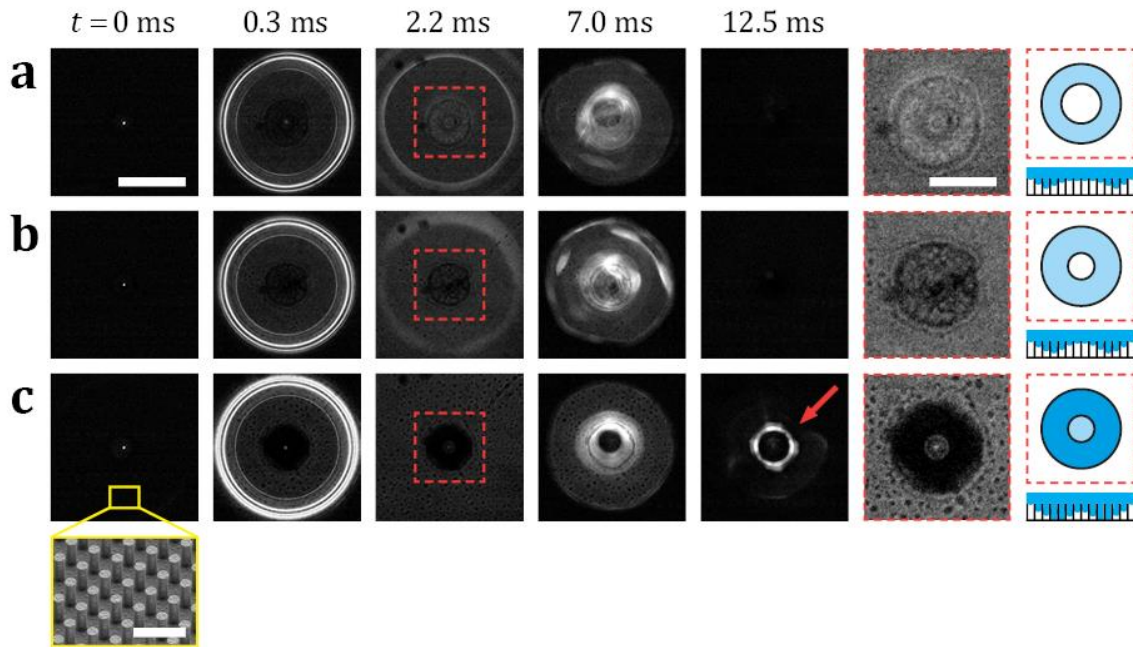
Figure 3. Bottom view impact sequences at low speed ($We = 48$). $[p, p_{v}] = [95, 1.3]$ kPa (a), $[p, p_{v}] = [2.5, \approx 0]$ kPa (b) and $[p, p_{v}] = [2.5, 2.3]$ kPa (c). Inset: SEM micrograph of iCVD-coated PUA micropillars $[d, s, h] = [2.5, 5.0, 5.8]$ μm. **(a)** Partial impalement with entrained bubble; full rebound observed ($\Phi = 0$, $n = 6$). **(b)** Partial impalement with smaller entrained bubble; full rebound observed ($\Phi = 0$, $n = 14$). **(c)** Full impalement with small entrained bubble; daughter droplet visible on surface after contraction ($\Phi = 0.85$, $n = 13$). Right side: magnified bottom views of red framed regions and, based on this, extrapolated side view schematics of meniscus penetration at maximum droplet spreading; ~ 2.2 ms after impact. Sequences are synchronised to first moment droplet appears in focus (white dot in centre of frame). Scale bars: (a)-(c) 1 mm; inset in (a)-(c), 0.5 mm; micrograph 10 µm.
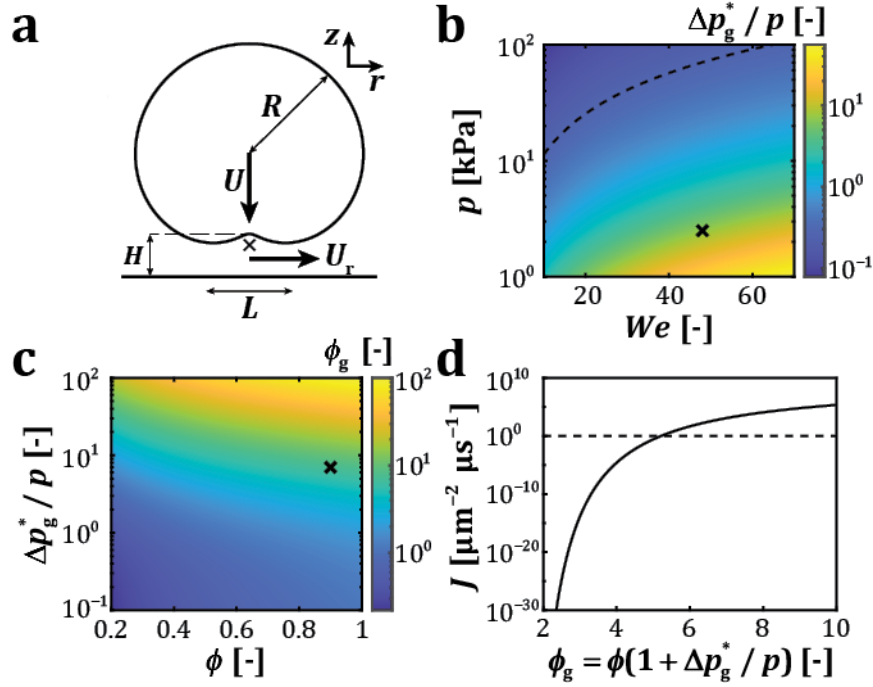
Figure 4. Condensation-based impalement model. **(a)** Schematic of the droplet with dimple (not to scale) immediately before impact. The increases in gas pressure and temperature, Δp_g and ΔT_g respectively, are calculated immediately beneath the droplet in the region denoted by the 'x'. **(b)** $\Delta p_g^*/p$ of gas entrained by the droplet at impact for fixed $R = 1.03$ mm, $\sigma = 0.072$ N m^{-1}, $\rho_l = 998$ kg m^{-3} and $\mu_g = 1.83\times10^{-5}$ Pa s. The relative pressure increase can be seen to be very small for all but low p and high We. The dashed line corresponds to the compressible limit above which, $\varepsilon > 1$ and is treated as $\varepsilon = 1$ for the calculation of Δp_g^* in Equation (2) **(c)** Plot of the supersaturation in the intervening gas layer, ϕ_g, across a range of ϕ and $\Delta p_g^* / p$. The 'x' symbol in (b) and (c) corresponds to the experimental conditions in Figure 3c yielding $\Delta p_g^* / p \approx 7$ and $\phi_g \approx 7.2$. **(d)** Plot of J vs. ϕ_g for a flat area of sample. $J \geq 1$ μm^{-2} μs^{-1} corresponds to a high likelihood of a nucleus growing on the surface. For one nucleus per micropillar unit cell, $J \geq 1\times10^{-2}$ μm^{-2} μs^{-1} is required corresponding to $\phi_g \approx 5$.
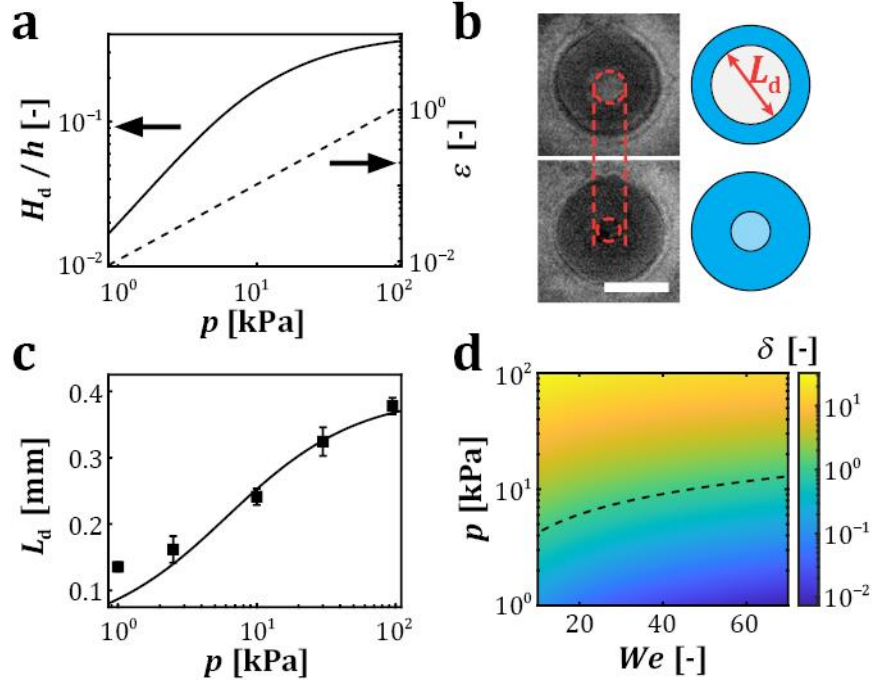
Figure 5. Pressure-based impalement mechanism analysis ($We = 63$). **(a)** Plot of H_d/h *vs.* p at impact (solid line) predicting decreased dimple size at lower p as we enter a more compressible regime (decrease in ε, dashed line). **(b)** Bottom view images and schematics for impalement at $We = 63$ for $p = 95$ kPa (top) and $p = 2.5$ kPa (bottom). L_d decreases for lower p ($L_d = [0.32 \pm 0.04, 0.16 \pm 0.02]$ mm respectively). **(c)** Plot of L_d *vs.* p for impalement at $We = 63$. Bottom view measurements (squares, $n = 3$; error bars represent one standard deviation of uncertainty, hidden by marker for $p = 1$ kPa) can be fitted to the scaling $L_d = a(RH_d)^{1/2}$ with $a = 8$ (solid line) and H_d, a function of p, calculated from Equation 1. **(d)** Plot of the gas cushion thickness coefficient, $\delta = H_d / \lambda$, across a range of p and We. The dashed line represents $\delta = 1$; below which, the likelihood of impalement is increased by the absence of a significant air cushion beneath the droplet on impact. Scale bar: (b) 0.5 mm.
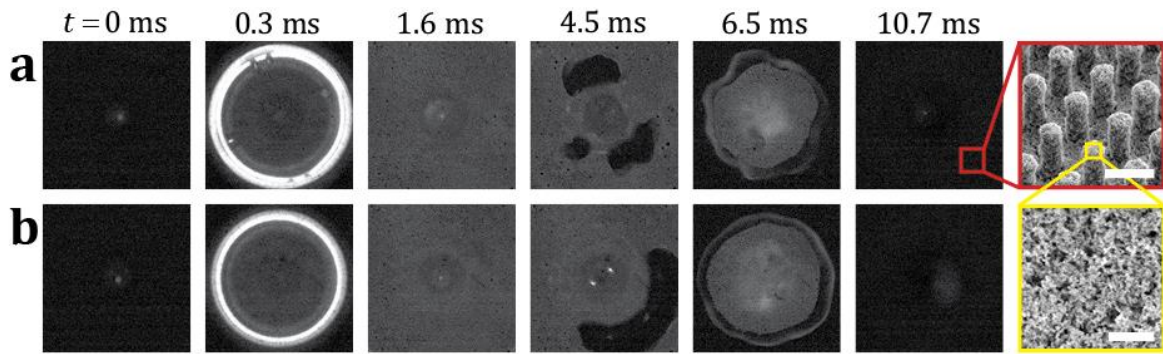
Figure 6. Bottom view impact sequences for hierarchical micropillars ($We = 63$). $[p, p_v] = [2.5, \approx 0]$ kPa (a) and $[2.5, 2.3]$ kPa (b). ($\Phi = 0$, $n = 5$ for both cases.) Inset in **a**: micrograph of hierarchical micropillars $[d, s, h] = [2.5, 5.0, 5.8]$ μm and added nanotexture. Scale bars: (a)-(b) 1 mm; inset in (a), 5 μm, 500 nm.